Society of Petroleum Engineers

SPE-196657-MS

Machine Learning for 3D Image Recognition to Determine Porosity and Lithology of Heterogeneous Carbonate Rock

Omar Al-Farisi, Hongtao Zhang, and Aikifa Raza, Khalifa University of Science and Technology; Djamel Ozzane, ADNOC; Mohamed Sassi and TieJun Zhang, Khalifa University of Science and Technology

This paper was prepared for presentation at the SPE Reservoir Characterisation and Simulation Conference and Exhibition held in Abu Dhabi, UAE, 17 - 19 September 2019.

Abstract

Automated image processing algorithms can improve the quality and speed of classifying the morphology of heterogeneous carbonate rock. Several commercial products have worked to produce petrophysical properties from 2D images and with less extent from 3D images, relying on image processing and flow simulation. Images are mainly micro-computed tomography (μCT), optical images of thin-section, or magnetic resonance images (MRI). However, most of the successful work is from the homogeneous and clastic rocks. In this work, we have demonstrated a Machine Learning assisted Image Recognition (MLIR) approach to determine the porosity and lithology of heterogeneous carbonate rock by analyzing 3D images form μCT and MRI. Our research method consists of two parts: experimental and MLIR. Experimentally, we measured porosity of rock core plug with three different ways: (i) weight difference of dry and saturated rock, (ii) NMR T_2 relaxation of saturated rock, and (iii) helium gas injection of rock after cleaning and drying.

We performed MLIR on 3D μCT and MRI images using random forest machine-learning algorithm. Petrophysicist provided a set of training data with classes (i.e., limestone, pyrite, and pore) as expert knowledge of μCT Image intensity correspondence to petrophysical properties. MLIR performed, alone, each task for identifying different lithology types and porosity. Determined volumes have been checked and confirmed with three different experimental datasets. The measured porosity, from three experiment-based approaches, is very close. Similarly, the MLR measured porosity produced excellent results comparatively with three experimental measurements, with an accuracy of 97.1% on the training set and 94.4% on blind test prediction.

Introduction

Quality static and dynamic reservoir properties determination and integration via micro and nano-imaging with machine learning aided image recognition (Dietterich 2000, Decencière et al. 2013, Arganda-Carreras et al. 2017, Sommer et al. 2011) is a challenging task. The current literature review has revealed the pressing challenges of the need to perform 3D image processing instead of 2D (Sánchez et al. 2008, Li and

Chutatape 2004) (Bovik 2009). Dual-energy micro-computed tomography (μCT) scanning data are used to characterize the rock properties (Rafael et al. 2007) (Saxena et al. 2017, Dernaika et al. 2018), claiming reasonable matching between measured core plug helium porosity and calculated using digital rock physics methods, and the same for permeability. The only drawback is no blind test; instead, the work appeared as a learning and exploring μCT abilities. This work suggests that a 2D image cannot predict the petrophysical properties in carbonate due to the limited representation of heterogeneous rock, such as carbonate. Lately, major oil operator stated no commercial vendor is yet able to measure the porosity and permeability, and for carbonate, it is even harder. In work performed (Chhatre et al. 2017) to check four DRP (Digital Rock Physicis) vendors' capabilities, the findings suggest no vendor managed to get Porosity, Permeability, and Pc (Capillary Pressure) curves correctly. The work also recommended that future DRP analysis should report the uncertainties. Then we investigated Artificial Intelligence, mainly machine learning software, used to perform rock properties' characterization (Alqahtani et al. 2018), by analyzing μCT images, where segmentation is a method for porosity calculation. Then a convolutional neural network (CNN) is used to get the pore size distribution. Alqahtani (Alqahtani et al. 2018) used 2D images, reminding us of the thin-sections analysis. Alqahtani (Alqahtani et al. 2018) paper can be useful as a procedural reference for conducting 2D image analysis. The paper also highlights using open-source ImageJ software (Collins 2007) and Tensor Flow software (Abadi et al. 2016). Image with 3D analysis was performed by (Dong and Blunt 2009), using μCT images and an approach called Maximal Ball algorithm. In Dong paper, the topological extraction of the pore network is evident. The primary importance of this paper is the connectivity between each pore, knowing that quantifying connectivity is essential to calculate rock dynamic properties. Dong work also put a way forward to build a dynamic property estimator for relative permeability and capillary pressure. Alqahtani (Alqahtani et al. 2018) paper also highlighted the effect of vugs that acts as large channels or high connectivity between matrix porosity. NMR is the best porosity logging measurement in the oil industry (Xu et al. 2015), as it is lithology independent. For a fully saturated core plug (like oil or water), the NMR signal represents porosity. While if water (or oil) saturated core contains another fluid (gas), then the gas is invisible to NMR. So in the case of CO_2 flooding, the NMR will act as a fluid saturation tool. In (Liu et al. 2016) work focused on NMR for saturation measurement, the paper showed the relation between relaxation time and pore size (Ausbrooks et al. 1999). The same methods were used earlier (Marschall et al. 1995). Carbonate is complex to characterize using image analysis as per Saxena (Saxena et al. 2017), as part of the work on sandstone and carbonate image processing for determining porosity and permeability. The work concluded that image processing, Saxena (Saxena et al. 2017), suits clastics only due to low heterogeneity. We have realized that achieving our goal requires an interdisciplinary approach, because an amalgamated knowledge of fluid dynamics, reservoir characterization (rock typing and petrophysical analysis), image processing, machine learning, and software coding is vital to deliver the solution. Our research deployed new analysis and verification approaches in the oil industry including 3DMM (3D Micro Models) with various micropore sizes, and use 3DMM as image processing calibration reference. Besides, a new image resolution enhancement for quality segmentation is developed. In our paper, we determined porosity using mainly two methods. The first is a standalone image processing (Abràmoff et al. 2004, Russ 2016), where image information extraction was successful. The second, is machine learning assisted image recognition (MLIR). These methods we built depending on the learning we gained from our experimental results. The difference between image processing and image analysis (Russ 2016) is important to distinguish. If image processing enables us to extract meaningful data, then image analysis is the ability to interpret this data via numerical analysis. Figure 1 highlights the schematics of the research work. We define Machine Learning as the ability of a machine to perform, learned tasks as good as the training set, on new data, faster and more accurate than a human expert, while the machine is still not smarter than human. In more engineering sense, the definition stepwise appears like the following:

1. Step 1: Input to machine a training data set of a knowledge domain.

2. Step 2: Human domain expert selects for the machine one or more learning algorithms.
3. Step 3: The machine performs the learning task from the provided data using the selected algorithms to build a model and test the model to know model accuracy. The model is appropriate for classification or regression prediction problems.
4. Step 4: The machine uses the model developed in step 3 above on new data set to perform the prediction.

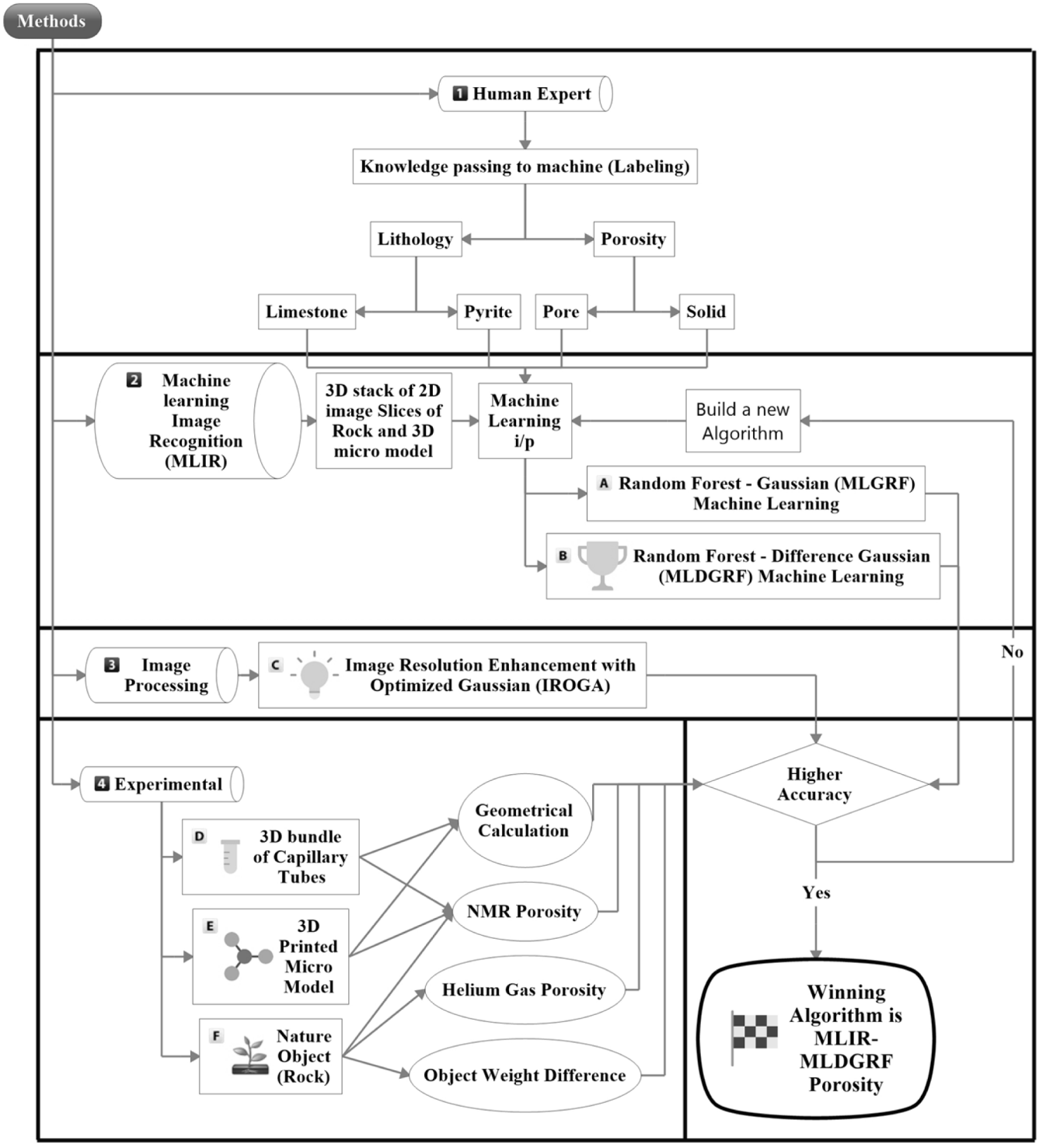

Figure 1—Our Method of 3D MLIR Porosity Determination and Verification Algorithm

1st Challenge: Resolution Effect on 3D uCT Images

Image resolution (Yang et al. 2010) is one of the main challenges in 3D morphological (Huang et al. 2008) recognition process. Naturally, better resolution leads to better segmentation (Drexler et al. 2001, Schindelin et al. 2012). However, not every image comes with the needed resolution for optimal image analysis. In 3D rock images, identifying 10^6s of micro-pores (void space) and quantifying their morphology (Gerke et al. 2015, Ehrlich et al. 1984, Singh et al. 2017) are pressing challenges. The resolution does blur the feature of interest. Numerically, the pixel color value does not represent the actual value. We acquired 3D uCT images for dry (pore contains air only) carbonate rock, and we displayed one of the 2D slices is in Figure 2. We could see, in Figure 2, how micro-pores in carbonate rock appear in more than one gray value, although it should appear as black. The cause of this challenge is low resolution, where the pore size is smaller than the pixel resolution that we acquired the image. The Pore must be black color (as air fills pores), where the pixel holds a value of "0". To accurately measure porosity, we must correct images to be "0" value for pore. The challenge is how to do correction without mistakenly converting true-non-void to void. In Figure 2, the Top image shows a 38 mm diameter sample acquired with 40 um resolution (each pixel is 40 × 40 um). The image inside the red circle is our zone of interest for identifying pore (Black) and solid (Light color). To solve the resolution effect, we innovated a convolutional Gaussian kernel for improving the resolution of 3D images, which we detailed in this paper.

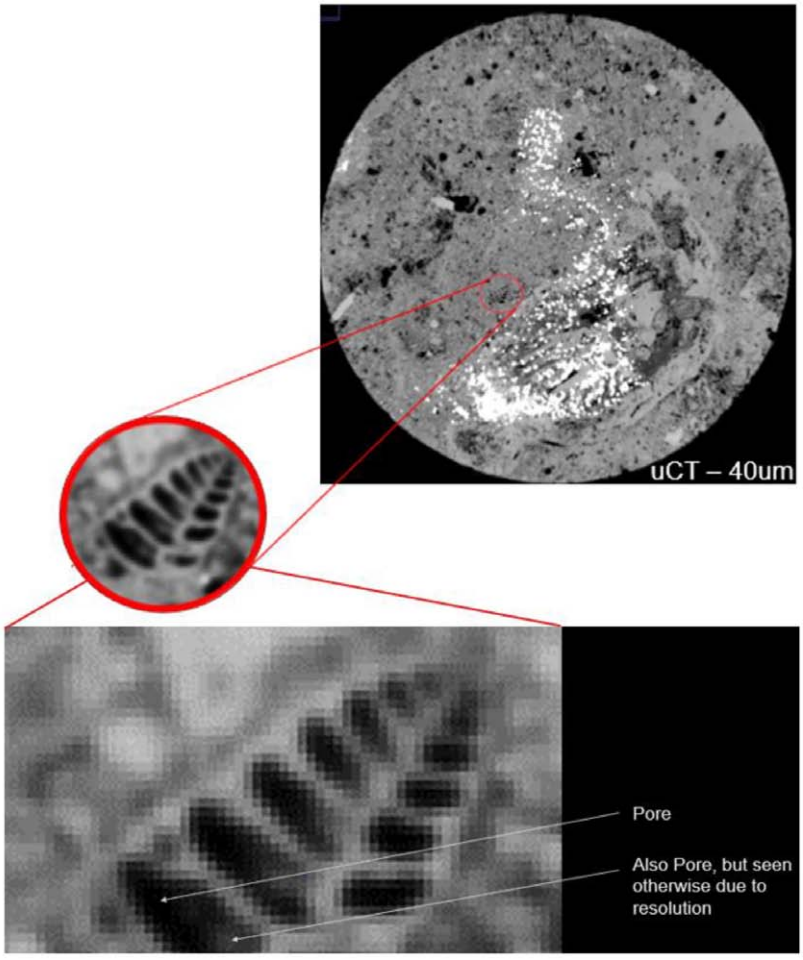

Figure 2—Resolution effect is evident in three different zooming scales.

2nd Challenge: Resolution Effect on 3D MRI Images

To identify the fluid distribution in the pore spaces, MRI would be one of the preferable options (Wang, Lun, et al. 2017, Zhou et al. 2001). For the same carbonate rock, we acquired 3D MRI images. The void in MRI appears lighter color, while solid appears as dark (Black). We flooded the pores of this rock sample with crude oil. Figure 3 shows three MRI cross-section images for this carbonate. We acquired the 3D MRI images with three different sampling rates. By different sampling rates, we mean different slice thickness along the z-axis, which is along with the core sample cylindrical shape. Images are (400 × 400 um) resolution, while slice thickness along z-axes (along core plug cylinder z-axis) is; 3.5mm (equivalent to 3500 um), to be (400 × 400 × 3500 um) for Left image. While it is 2.5 mm (equivalent to 2500 um) for Middle image, (400 × 400 × 2500 um). And 1.5 mm (equivalent to 1500 um) for Right image, (400 × 400 × 1500 um). It is important bringing right-side image (thinner 2D MRI slice, or higher resolution in the z-axis), in Figure 3, to be clear as the left image (thicker 2D slice or lower resolution in the z-axis), for monitoring fluid behavior inside microporous media. The left image has a higher dynamic range of intensity despite its lower z-axis resolution.

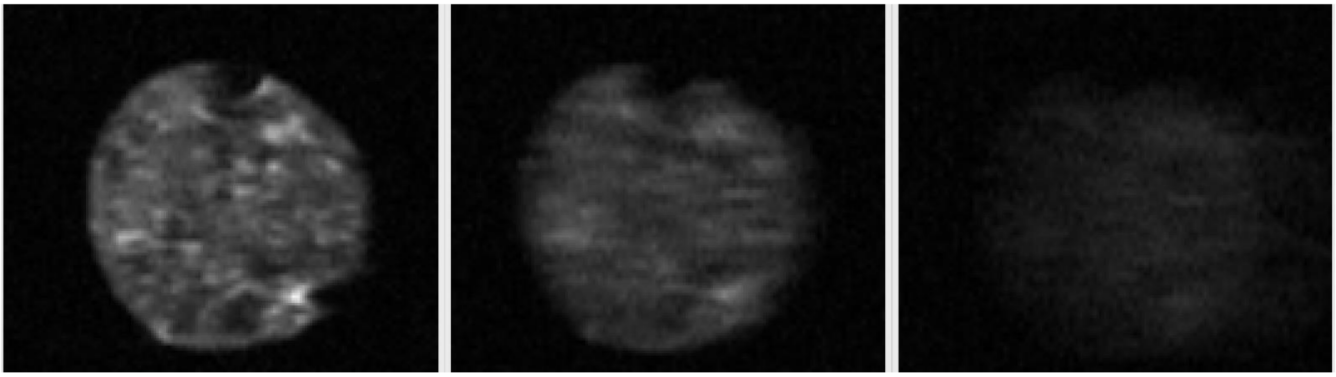

Figure 3—MRI images for the core plug with three different sampling rates.

Resolution Enhancement Solution

To solve for the resolution effects, we launched an experimental task that involves building 3D micro models, as shown in Figure 1. We created several types of micro models to enable quantifying the blurriness of the image and correct for it. To increase resolution, reducing the blurriness effect, we needed to build an image correction model, and at the same time, we had to ensure efficiency. Therefore, a convolutional Gaussian image processing filter (Li et al. 2018, Buades et al. 2005), was the first choice we worked. After several trials and error, we managed to develop a novel Optimized Convoluted Gaussian image processing algorithm. We called the new algorithm IROGA (Image Resolution Optimized Gaussian Algorithm).

The Methodology of Machine Learning Assisted uCT/MRI Image Recognition (MLIR)

Machine Learning

In our research, we have followed the four steps sequenced below:

1. Step 1: Human expert (Geoscientist), a petrophysicist in our case, provided data set to the machine. Our petrophysicist identified two types of minerals (limestone and pyrite), two physical statuses (pore and solid), and four image intensities (Chen et al. 1998, Collewet et al. 2004, Shattuck et al. 2001, Wang, Aghaei, et al. 2017 The data set contains:

i. "Independent parameters data columns"; image identified properties with black color, dark gray intensity, light gray intensity, and white.
ii. "dependent data column"; containing the desired classes of Limestone, Pyrite &Pore, while Solid here represents an aggregation of both Limestone and Pyrite.

2. Step 2: Human Expert chooses a Machine Learning Algorithm (Pedregosa et al. 2011) that are available as open-source; in our case we found the "Random Forest" algorithm (Breiman 2001) to be the best, owing to its superior capability in performing Classification.
3. Step 3: The Computer (Machine) uses the Random Forest algorithm to learn from the data set and build the Prediction Model with all its Governing Equations (Yu et al. 2016).
4. Step 4: The Computer uses input data set, 3D μCT Image and MRI image, and uses the learned Prediction Model with its Governing Equations to predict output classes.

Image Processing

We define Image Processing as tasks a human expert performs on the image (2D, 3D, 4D or 5D) that produce a new set of information or new image version that provides more insight into a human expert. In more engineering sense, the definition stepwise appears like the following:

1. Step 1: Input to machine an image (2D, …, 5D), as 2D represents space (gray or colored), 3D represents the volumetric view (Zhang et al. 2006, Deriche 1987, Dunlavy et al. 2008, Calliess et al. 2012).
2. Step 2: Domain expert selects and runs suitable filtering, segmentation, and analysis algorithms (Malcolm et al. 2007, Lindquist et al. 1996, Ehrlich et al. 1984, Lindquist and Venkatarangan 1999, Mowers and Budd 1996) to achieve the image-processing objectives.
3. Step 3: The human expert learns new insight and generates new data (numerical or image) because of step 2 above.

Another definition of Image processing is, (Gonzalez et al. 2009) "…Image Processing encompasses processes whose inputs and outputs are images and, besides, encompasses processes that extract attributes from images, up to and including the recognition of individual objects."

Combining Machine Learning and Image Processing

The combination scenario we called it Machine Learning Image Recognition (MLIR), which we define as "the ability of a machine to perform tasks" (Kann et al. 2019) as good as training set, image interpretation, delivered by a human expert, on new images faster and more accurate than human expert but not smarter than a human expert. Another definition also describes Machine Learning and Image Processing (Gonzalez et al. 2009). Image recognition via machine learning (He, Zhang, et al. 2016, Simonyan and Zisserman 2014) requires more time when we compare it to the time needed with image processing. In this paper, we discussed what type of methodology to use and the reasoning behind it.

Porosity Determination

We measured Porosity, for rock core plug, using Helium gas (Jones 1987, 1986), and this what we consider as the ultimate reference of porosity value. Also, we imaged the same core plug. In our research, we imaged the rock with uCT and MRI (Magnetic Resonance Imaging) (Wang, Lun, et al. 2017). In our study, the porosity determination method consists of two parts: Experimental and Machine Learning Image Recognition (MLIR).

Porosity from Experimental Measurements

In the experimental part, we measured core plug porosity with three different measurement methods. The first measurement method is with weight difference (Luffel and Guidry 1992) of rock under dry and wet conditions. In the second measurement method, we used NMR (Coates et al. 1999) on the same rock saturated with fluid (crude oil). The third method is made with helium gas (Jones 1987, 1986), on the same rock sample after cleaning and drying.

Porosity from Machine Learning

In the machine learning part, we performed 3D uCT image recognition using random forest machine-learning algorithm. The primary Machine Learning performed tasks were as per the following process:

1. Human Expert (Geoscientist), a Petrophysicist in our case, provided data set to Machine. Our Petrophysicist identified two types of minerals (Limestone and Pyrite), two physical statuses (Pore and Solid) and four image intensities. The data set contains:
   i. "Independent Parameters data columns"; Image identified properties with Black Color, Dark Gray Intensity, Light Gray Intensity, and White (Felzenszwalb and Huttenlocher 2004, Ashburner and Friston 2005).
   ii. "Dependent Data Column"; containing the desired classes of Limestone, Pyrite & Pore. Solids here include the Limestone and Pyrite.
2. Human Expert chooses a Machine Learning Algorithm; in our case, we selected the "Random Forest" algorithm owing to its superior capability in performing Classification.
3. The Computer uses the Random Forest algorithm to learn from the data set and build the Prediction Model with all its Governing Equations.
4. The Computer inputs new data set, 3D uCT Image, and uses the learned Prediction Model with its Governing Equations to predict output classes.

In this research we used mainly three software; Microsoft Office 365™ Excel (Wilson 2014), Python (Müller and Guido 2016) and Imagej (Ferreira and Rasband 2012) for Machine Learning, Image Processing, Mathematical Modeling, and Graph Generation.

Experiment Design and Imaging for Bundle of Capillary Tubes 3D Micro Model 3DMM

We realized that without proper measurement control, the complexity of interpreting image data (uCT and MRI) would continue without a solution. Therefore, in our research, we developed 3D Micro Model (3DMM) with various micropore sizes to use them as measurement control.

Types of 3DMM

The micro model we developed are three types:

1. Bundle of Capillary Tubes 3D Micromodels.
2. Glass Beads 3D Micro Models.
3. Multi-Geometry 3D Micro Models.

Dimensions of the Bundle of Capillary Tubes 3DMM

We built a 3D micro model (3DMM) with known dimensions of pore and solid, 26 tubes, the length is 2" (50.8 mm), while the tube inner-diameter is 600 um. The 3DMM enabled constructing and verifying IROGA in a controlled environment. The 3DMM is in Figure 4, with its cross-sectional and longitudinal structure.

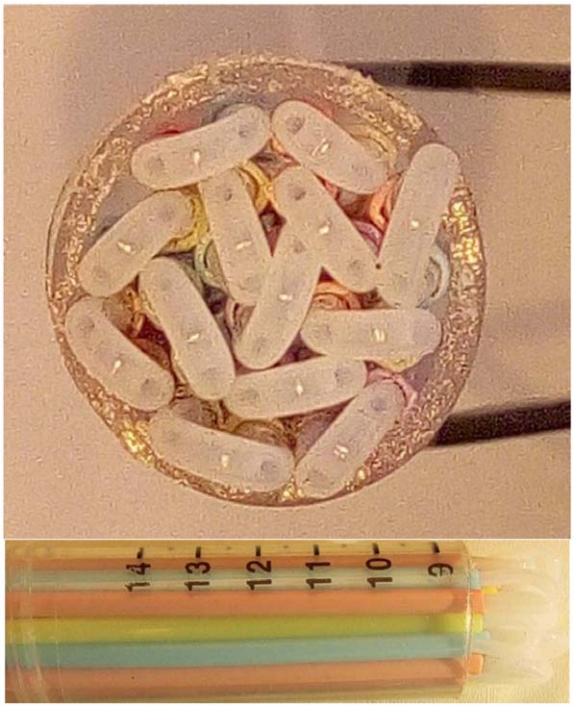

Figure 4—3D physical micro model with the cross and longitudinal sections. MRI images of this model trained and tested IROGA.

3DMM Imaging and Calculations

The calculated Porosity is 7.21%. We used 0.5 Tesla MRI device. We collected 3D MRI stack, which consists of nine 2D slices, as shown in Figure 5. In looking to Figure 5, the small light dots represent void (Pore), while black represents solid, and the gray color rectangles represent the separators between each 2D image slice. Each dot represents one tube. We enlarged one of the nine MRI 2D slices, as shown in Figure 6.

Figure 5—3D MRI cross-section images of nine 2D slices for the 3D micromodel.

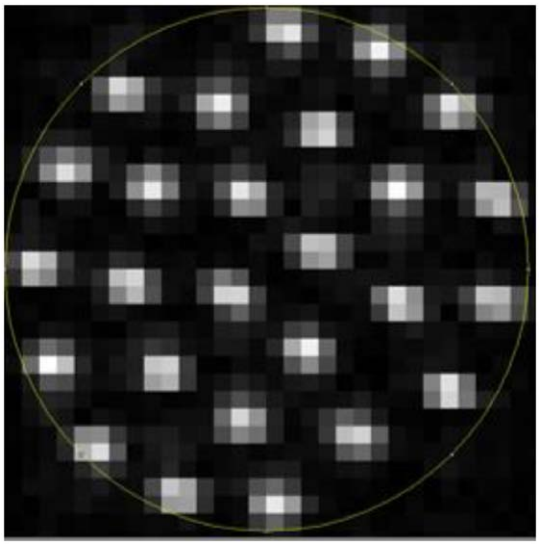

Figure 6—Enlarged MRI slice showing unwanted resolution defect in gray shade.

Running 3DMM Experiments for Constructing IROGA

To perform this task, we designed and conducted experimental screening of three different methods. As discussed earlier, two machine learning methods and one novel image-processing algorithm. The list below shows these three methods which we will describe subsequently:

a. The First Method: Machine Learning Gaussian Random Forest.
b. The Second Method: Novel IROGA Image processing algorithm.
c. The Third Method: Machine Learning Difference Gaussian Random Forest.

The First Method: Machine Learning Gaussian Random Forest (MLGRF)

We used the traditional Gaussian (Rasmussen 2003) Random Forest (Polan et al. 2016) as part of open-source ImageJ software (Abràmoff et al. 2004). We trained MLGRF algorithm with data set generated via interactive labeling using human expert knowledge, Petrophysicist in our case. Then we selected the Gaussian function to build the best representative model and perform the classification. In Figure 7(a), the black and white MRI image is the raw acquired image of (400 × 400 um) resolution. The model generated Figure 7(b) with red and green colors. We notice void (pore area) is more significant than our reference, and accuracy is 53.1%, which is not acceptable.

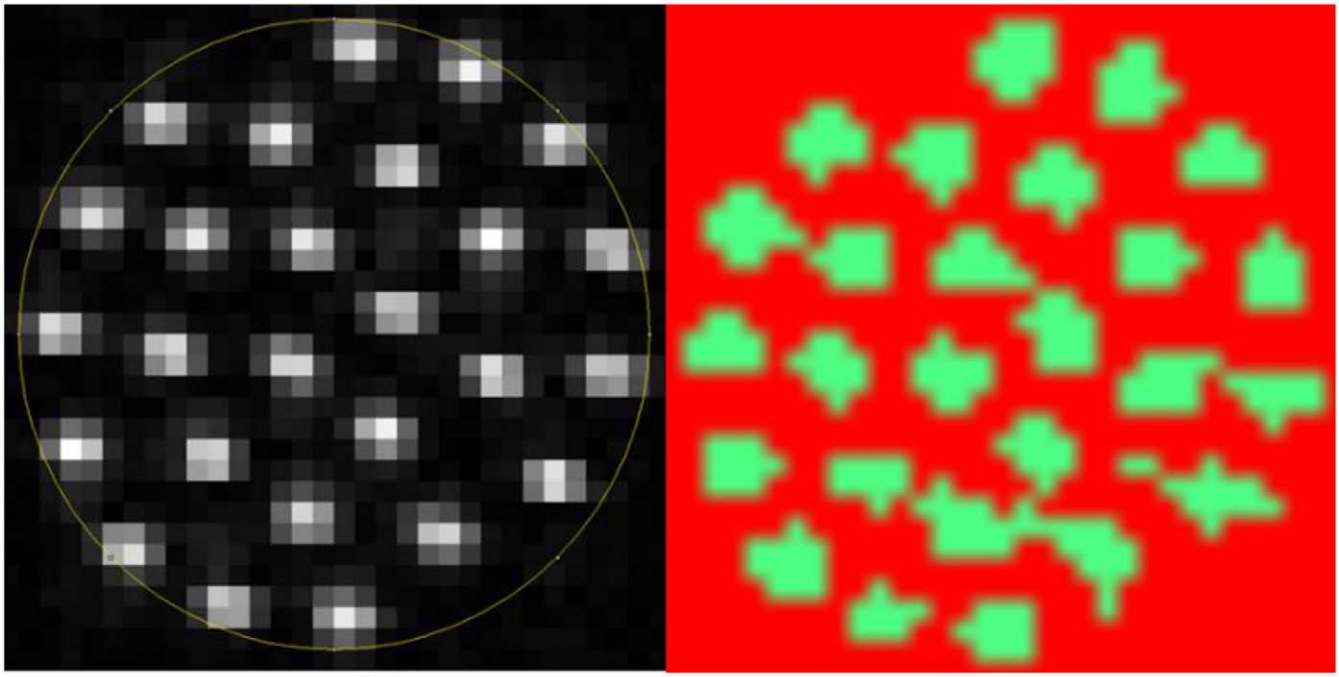

Figure 7—Cross-section of a 2D slice for 3D MRI image stack.

The Second Method: Novel IROGA (Image Resolution enhancement with convoluted Optimized Gaussian Algorithm)

A universal image enhancer may provide an easy way for processing future MRI images without the need for human expert labeling; that is what we thought and then innovated. 3DMM MRI images enabled producing universal image resolution enhancement, for similar temperature, signal strength, and acquisition parameters. We constructed IROGA, as shown in Figure 8. IROGA is an image-processing algorithm that can replace machine learning image recognition for segmenting two clusters. While segmenting (or interchangeably we use "classifying") more than two classes, then machine learning algorithms like the

random forest (Sommer et al. 2011) or others would be more suitable. Let us keep in mind that IROGA, as a standalone algorithm is useful when we target one or more of the following goals:

1. If we want to enhance the resolution of an image.
2. If we want to differentiate two labels (binary).
3. If we want to take (1) and (2) together.
4. Or if we want to determine porosity from a low-resolution image.

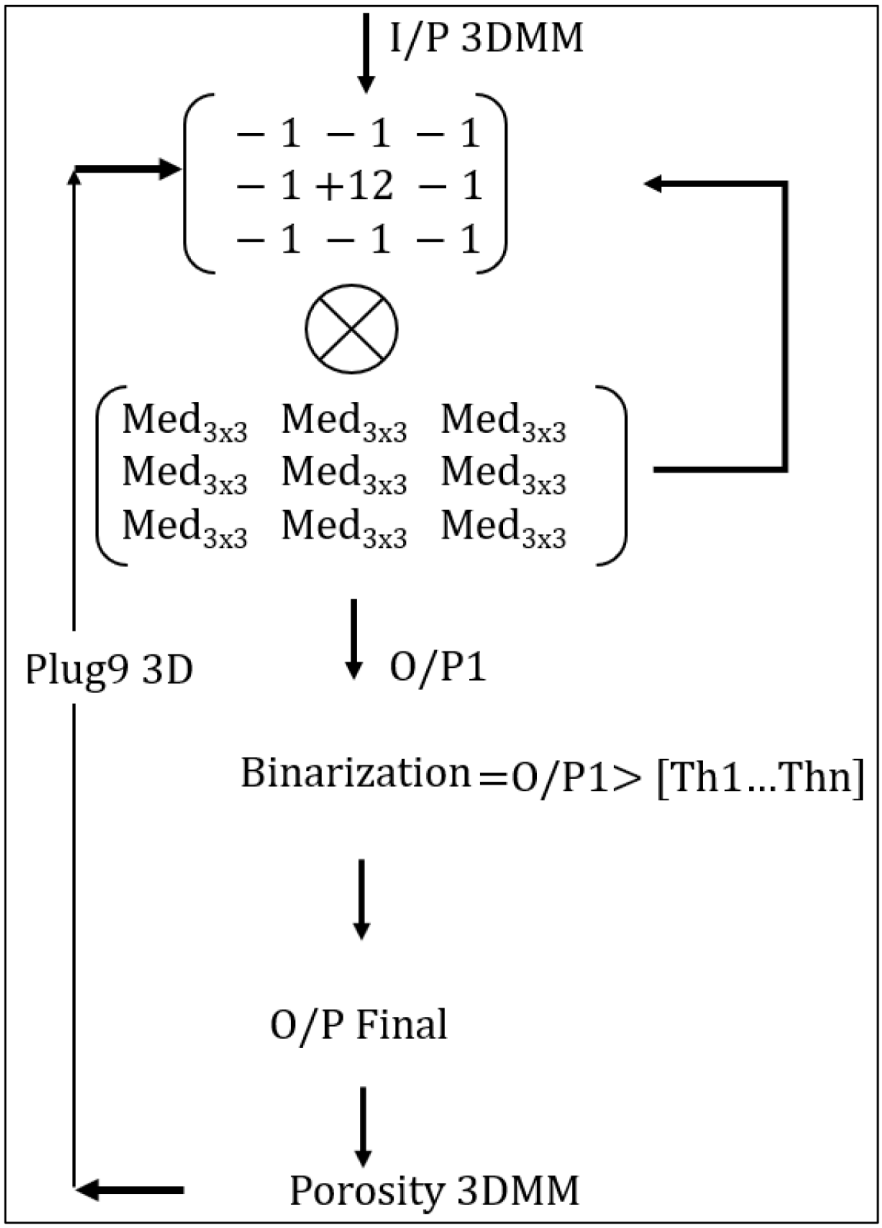

Figure 8—IROGA Algorithm Block Diagram.

We designed IROGA after several preliminary verification steps. IROGA has two action Loops, as shown in Figure 8:

1. IROGA Small Loop: Enhanced Convoluted Gaussian (ECG).
2. IROGA Large Loop, Image Processing Based Porosity Determination (IPBPD).

We constructed IROGA with continuous iterations by optimizing the gaussian values. Figure 9(a) shows the original raw MRI image of the 3DMM. Figure 9(c) is the final image of IROGA after applying the algorithm, while Figure 9(b) is the first IROGA iteration. We validated IROGA model, achieving high accuracy of IROGA, reaching to 96.2%.

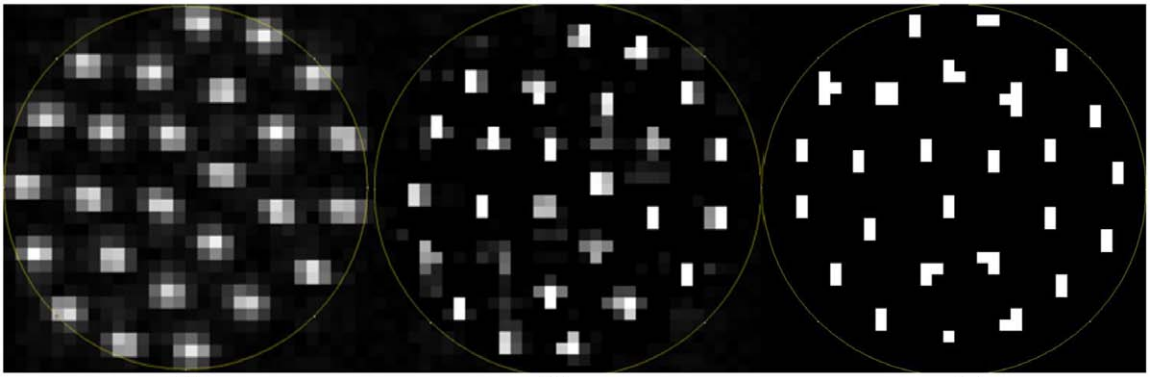

Figure 9—Cross Section of one of 2D slices of 3DMM MRI stack: (a) original image, (b) image after 1st IROGA iteration and (c) is the final image result.

The Third Method: Machine Learning Difference of Gaussian Random Forest (MLDGRF)

We used machine learning Random Forest, with a different algorithm than the First Method, this second algorithm is called Difference of Gaussian (Lindeberg 2015, Polakowski et al. 1997, Lowe 2004) Random Forest. In Figure 10(a), we see the original 3DMM MRI image; black color represents solid, and light color represents void (Pore). While in Figure 10(b) we see the enhanced resolution image using MLDGRF, where red color represents solid and green color represents Pore. MLDGRF produced higher accuracy of 97.1%, as the best method accuracy wise for resolution enhancement and porosity determination. By comparing IROGA with both MLIR methods, MLGRF and MLDGRF, we found Gaussian Random Forest MLGRF approach is the worst. While MLDGRF and IROGA showed the best results with 97.1% and 96.2% accuracy respectively. MLIR algorithm is in Figure 11. Besides, to see the difference between Gaussian and Difference of Gaussian Function, we plotted both functions in Figure 12.

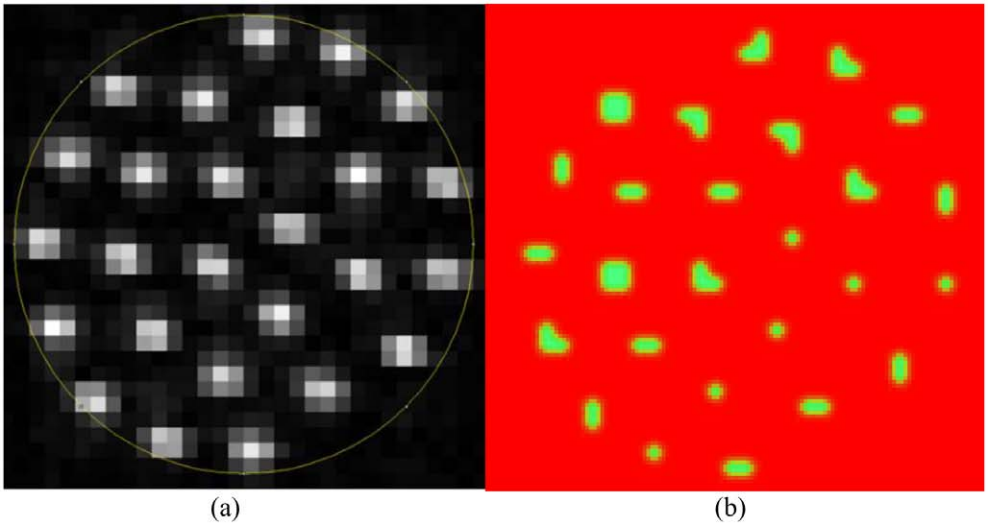

Figure 10—3DMM MRI image (a) is the original image. (b) is the enhanced resolution image using Machine learning Difference Gaussian Random Forest.

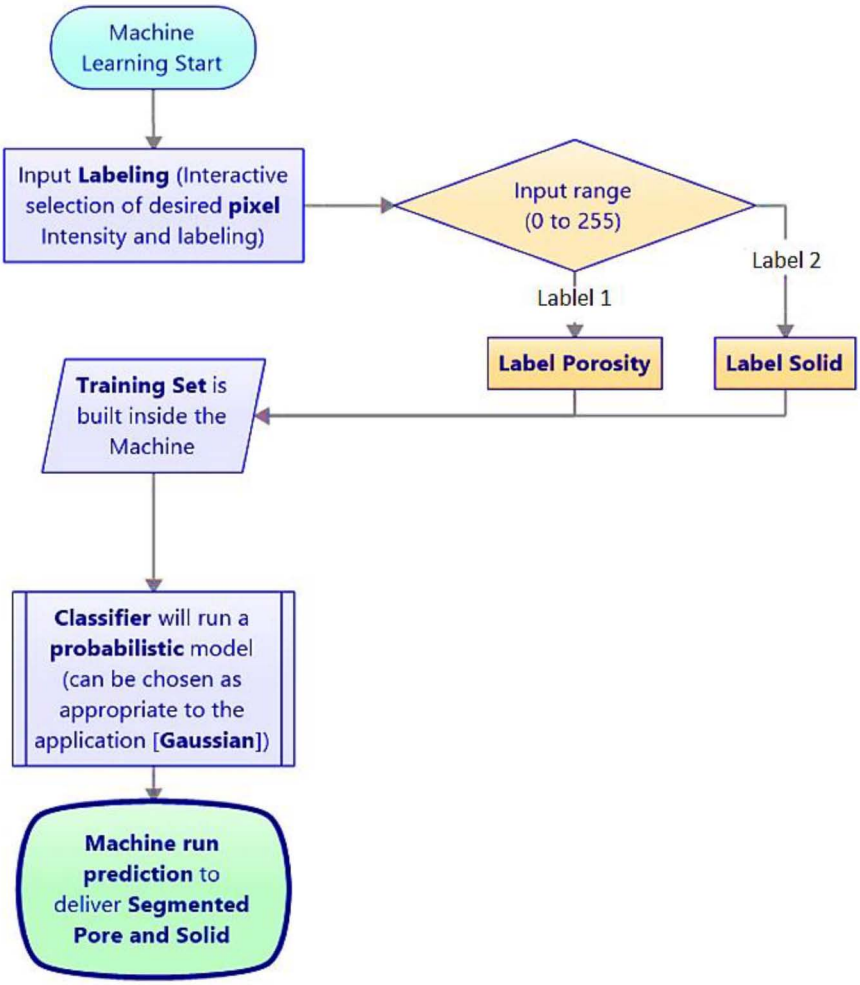

Figure 11—Machine Learning Random Forest.

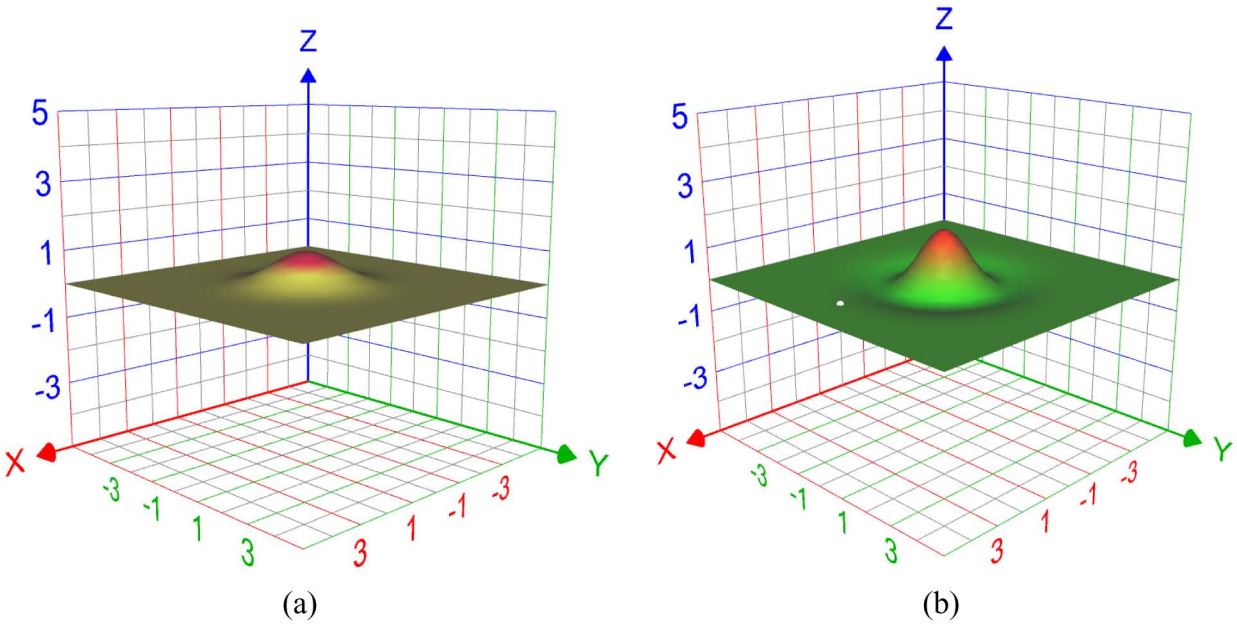

Figure 12—A 3D Graph of (a) Gaussian Function (b) Difference of Gaussian Function

IROGA Prediction and Validation for Carbonate Rock

We performed the prediction and validation of IROGA on carbonate core plug using MRI images. In Figure 13(a), we displayed raw MRI image of lower cretaceous carbonate rock, saturated with crude oil, black color represents solid and light color represents Pore filled with liquid. Figure 13(b) is the final MRI IROGA results;the red color is Solid, while the green color is Pore and filled with crude oil. For validating IROGA prediction, we used the reference Helium porosity, and the resultant accuracy is 91.8%.

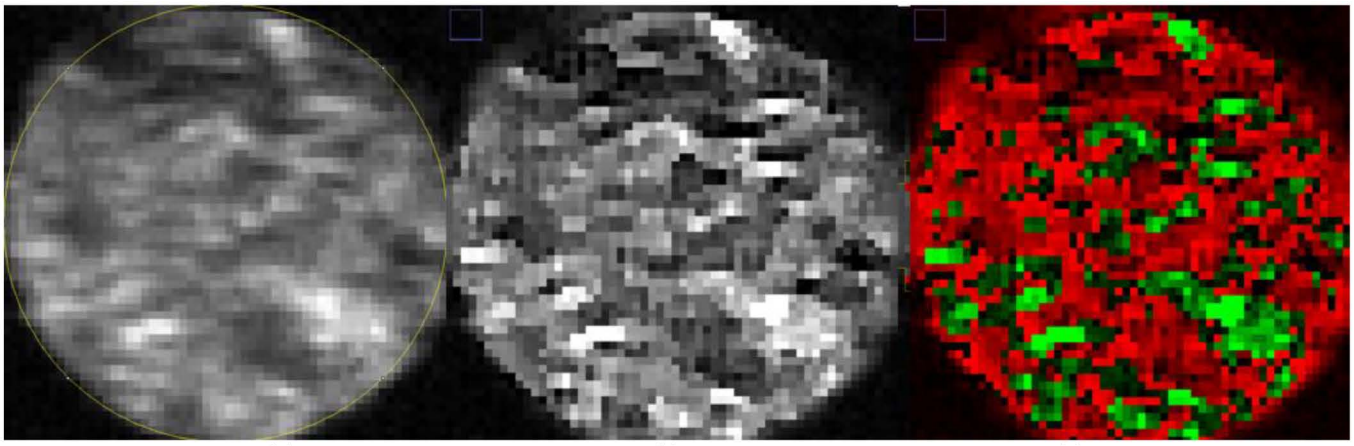

Figure 13—Lower Cretaceous Carbonate Rock MRI image (a) Raw image, (b) enhanced resolution image and (c) rock and oil separation.

We summarized below the experiment, modeling, and utilization of IROGA:

1. We built 3DMM with 600um inner diameter tubes.
2. We flooded 3DMM with Crude Oil collected from a lower Cretaceous Offshore Abu Dhabi formation.
3. We acquired 3D stack MRI Images (400 × 400 um) resolution for 3DMM.
4. We structured an iterative image resolution enhancement algorithm, depending on a convoluted Gaussian matrix.
5. We validated IROGA model with geometrical reference calculation of the 3DMM.
6. We acquired a 3D MRI Stack of a fluid-saturated carbonate rock core plug.
7. We applied IROGA on the core plug MRI image to measure porosity and located fluid distribution.
8. We validated IROGA porosity results with the reference Helium porosity.

3D μCT Carbonate Rock Machine Learning Image Recognition Porosity

Since we have shown the success of MLIR in achieving the highest accuracy when measuring 3DMM porosity, we extended the work to 3D μCT. We used MLDGRF algorithm to measure 3D μCT porosity. Results of MLDGRF uCT Porosity is in Figure 14(a). Then we compared MLDGRF results with three porosity measurements, as shown in Figure 14(b). The accuracy of MLDGRF reached 94.37%. The images of 3D μCT MLDGRF porosity predictionare in presented in Figure 15. We attribute the reason to have ~1.7pu (porosity unit) difference in porosity value between MLDGRF and the reference Helium porosity, to the Difference of Gaussian function. We recommend further tuning of the function parameters to increase the accuracy higher than 94.37%.

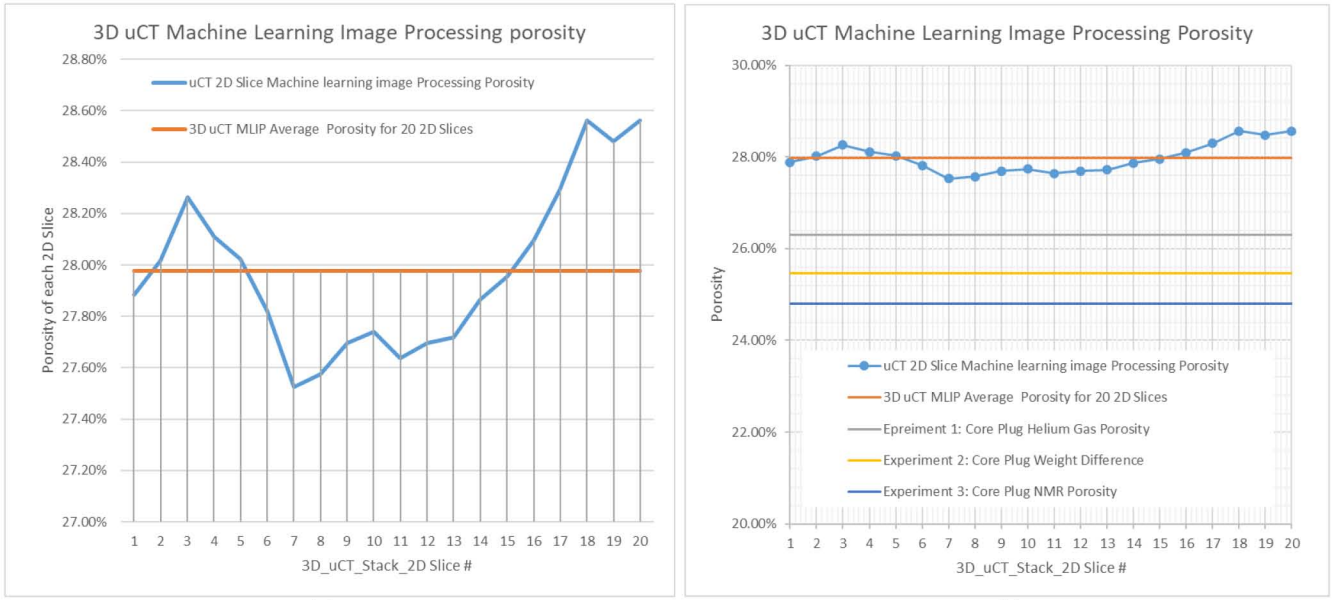

Figure 14—Lower Cretaceous Carbonate Rock (a) 3D uCT MLDGRF Porosity of 20 2D slices (b) Comparing 3D uCT MLDGRF Porosity with reference porosities.

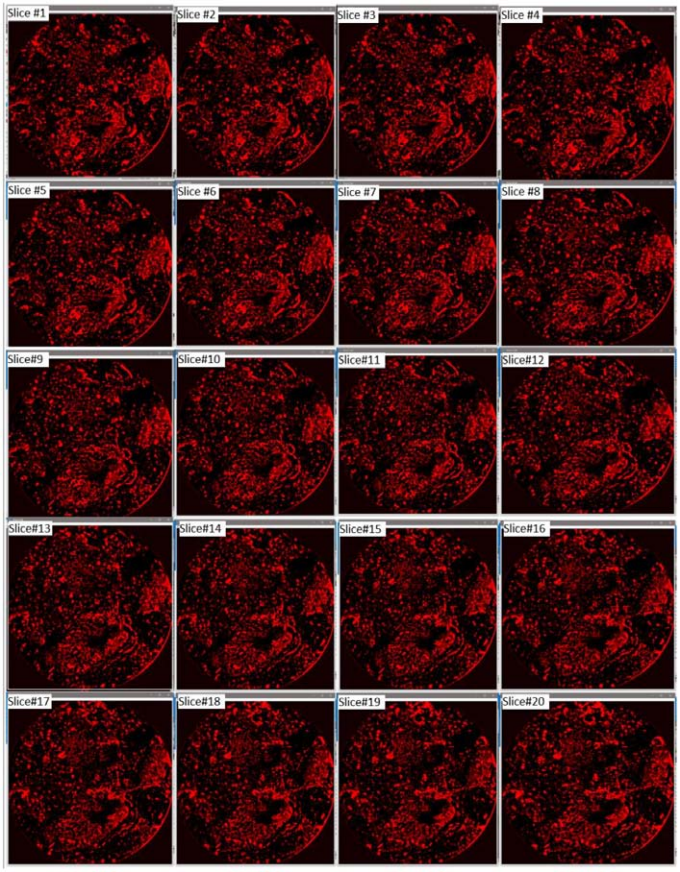

Figure 15—The Machine Learning Image Recognition MLDGRF predicted Porosity (red is pore) of 20 2D-slices of Carbonate Rock 3D uCT Stack image.

Identifying Lithology by MLIR

The vital step in performing rock typing as part of reservoir characterization study is to identify Lithology (Al-Farisi et al., Al-Farisi et al. 2009, Al-Farisi et al. 2013). In our research, human expert labeled different lithologies existing in 3D uCT stack, in our case, Pyrite and Limestone. Then MLDGRF algorithm is applied to differentiate the minerals in the rock, see Figure 16.

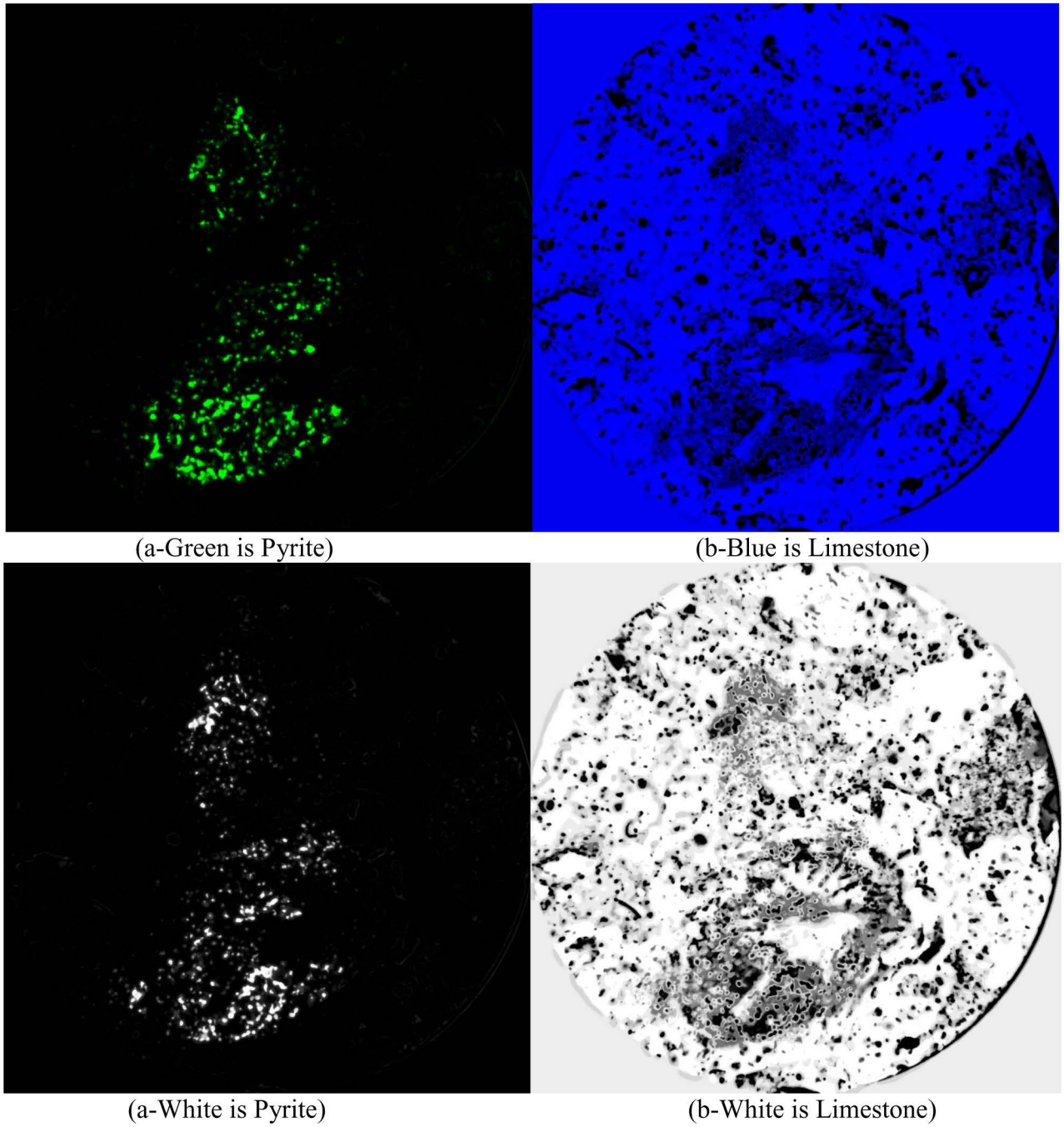

Figure 16—Machine Learning Image Recognition Difference Gaussian Random Forest algorithm MLDGRF has identified and segmented Lithology for 3D uCT Stack. Both (a-Green) and (a-White) are the same segmented image for Pyrite mineral, where Pyrite is the green color in (a-Green) image as the original segmentation image, and we displayed it again in (a-White) for printing purposes if the green image is not clear. While (b-Blue) and (b-White) are similar images for Limestone segmentation, where Limestone is the blue color in (b-Blue) image as the original segmentation image, and we displayed it again in (b-White) for printing purposes if the blue image is not clear.

Geoscientists have performed, during the last 40 years, mineral identification from images, even for outcrop rock (Kurz et al. 2012). We noticed that most of the studies have worked on borehole imaging rather than core plug uCT images (Knecht et al. 2003). Identifying and measuring minerals in core samples, currently, are mainly by physical weight measurements. While in using imaging for Lithology identification, either thin section or SEM images provided the primary source for mineral analysis (He, Ding, et al. 2016). In this study, we focused on 3D μCT images to be the source of Lithology identification and quantification, especially mineral segmentation and quantification. Also, most of the previous work has focused on the textural identification to determine lithofacies and other petrophysical properties (i.e., Archie's equation parameters and bioclast) (Knecht et al. 2003, Ketcham and Iturrino 2005, Knackstedt et al. 2007, Knackstedt et al. 2004). Therefore, our research has proven that Lithology (minerals) identification, segmentation, volumetric quantification, and precise locating are achievable. Figure 16 shows two different minerals that MLDGRF managed to segment, quantify, and locate.

Conclusions & Recommendations

1. To determine the reservoir properties (i.e., porosity and lithology), we investigated several methods and proposed a new one based on μCT and MRI images. We found that machine learning image recognition with Difference Gaussian Random Forest algorithm is superior compared to machine learning image recognition with Gaussian Random Forest algorithm. This finding will help us to choose the optimal machine learning algorithm for reservoir properties determination from various image types. Moreover, experimental validation is what we recommend, as it is a physical proof and the reference to quantify the algorithm accuracy.
2. Machine Learning Difference Gaussian Random Forest algorithm works well for a different type of images (i.e., μCT and MRI). If the domain expert correctly labels the desired features and chooses the best algorithm, machine learning image recognition can save years of tedious work. Therefore, machine learning is recommended in all oil and gas industry to produce quality results faster.
3. Improving the resolution of 3D MRI needs adequate image processing algorithms. Unless verifying algorithms, enhancement leads to over or under correcting. With experimental work, we developed a new image enhancement algorithm for binary (two classes) segmentation. Image processing can save time over machine learning for image recognition, where longer time is associated with a deeper machine learning algorithm. While for segmenting more than two classes, machine learning is better, especially with a heterogeneous rock.
4. Our work on porosity determination using machine learning has helped better understanding of rock heterogeneity and provided insight into analyzing our rock and classifying it digitally.

Acknowledgment

We want to thank ADNOC, ADNOC Offshore, and Khalifa University for permitting the publication of this paper as part of a joint research project and a Ph.D. thesis. Especially we thank the support of Mr. Saoud Almehairbi, Andreas Scheed, Ahmed Al-Riyami, Hamdan Al-Hammadi, and Khalil Ibrahim. We shall also extend our acknowledgment to Dr. Moustafa Dernaika (ADNOC), Mr. George Mani (Corelab), and Mr. Osama Jallad (Ingrain) for their support.

References

Abadi, Martín, Barham, Paul, Chen, Jianmin et al 2016. Tensorflow: A system for large-scale machine learning. Proc., 12th {USENIX} Symposium on Operating Systems Design and Implementation ({OSDI} 16)265-283.

Abràmoff, Michael D, Magalhães, Paulo J, and Ram, Sunanda J. 2004. Image processing with ImageJ. *Biophotonics international* **11** (7): 36-42.

Al-Farisi, Omar, Belhaj, Hadi, Ghedan, Shawket et al 2013. Carbonate Rock Types Matrix, the Ultimate Rock Properties Classification Catalogue. Proc., International Petroleum Technology Conference.

Al-Farisi, Omar, Elhami, Mohamed, Al-Felasi, Ali et al 2009. Revelation of carbonate rock typing—the resolved gap. Proc., SPE/EAGE Reservoir Characterization & Simulation Conference.

Al-Farisi, OU, Belgaied, AA, Shebl, HT et al Well Logs: The Link Between Geology and Reservoir Performance. *Abstract Geo2002* **96**.

Alqahtani, Naif, Armstrong, Ryan T, and Mostaghimi, Peyman. 2018. Deep learning convolutional neural networks to predict porous media properties. Proc., SPE Asia Pacific oil and gas conference and exhibition.

Arganda-Carreras, Ignacio, Kaynig, Verena, Rueden, Curtis et al 2017. Trainable Weka Segmentation: a machine learning tool for microscopy pixel classification. *Bioinformatics* **33** (15): 2424-2426.

Ashburner, John and Friston, Karl J. 2005. Unified segmentation. *Neuroimage* **26** (3): 839-851.

Ausbrooks, Robin, Hurley, Neil F, May, Andrew et al 1999. Pore-size distributions in vuggy carbonates from core images, NMR, and capillary pressure. Proc., SPE annual technical conference and exhibition.

Bovik, Alan C. 2009. *The essential guide to image processing*: Academic Press.

Breiman, Leo. 2001. Random forests. *Machine learning* **45** (1): 5-32.

Buades, Antoni, Coll, Bartomeu, and Morel, J-M. 2005. A non-local algorithm for image denoising. Proc., 2005 IEEE Computer Society Conference on Computer Vision and Pattern Recognition (CVPR'05)60-65.

Calliess, Jan-P, Mai, Michael, and Pfeiffer, Sebastian. 2012. On the computational benefit of tensor separation for high-dimensional discrete convolutions. *Multidimensional Systems and Signal Processing* **23** (1-2): 255-279.

Chen, E-Liang, Chung, Pau-Choo, Chen, Ching-Liang et al 1998. An automatic diagnostic system for CT liver image classification. *IEEE transactions on biomedical engineering* **45** (6): 783-794.

Chhatre, Shreerang S, Sahoo, Hemant, Leonardi, Sergio et al 2017. A Blind Study of Four Digital Rock Physics Vendor Labs on Porosity, Absolute Permeability, and Primary Drainage Capillary Pressure Data on Tight Outcrop Rocks. Proc., Oral presentation given at the Annual Symposium of the Society of Core Analysts, Vienna, Austria.

Coates, George R, Xiao, Lizhi, and Prammer, Manfred G. 1999. *NMR logging: principles and applications*, Vol. 234: Haliburton Energy Services Houston.

Collewet, G, Strzelecki, M, and Mariette, F. 2004. Influence of MRI acquisition protocols and image intensity normalization methods on texture classification. *Magnetic resonance imaging* **22** (1): 81-91.

Collins, Tony J. 2007. ImageJ for microscopy. *Biotechniques* **43** (S1): S25-S30.

Decencière, Etienne, Cazuguel, Guy, Zhang, Xiwei et al 2013. TeleOphta: Machine learning and image processing methods for teleophthalmology. *Irbm* **34** (2): 196-203.

Deriche, Rachid. 1987. Using Canny's criteria to derive a recursively implemented optimal edge detector. *International journal of computer vision* **1** (2): 167-187.

Dernaika, Moustafa, Al Mansoori, Maisoon, Singh, Maniesh et al 2018. Digital and Conventional Techniques to Study Permeability Heterogeneity in Complex Carbonate Rocks. *Petrophysics* **59** (03): 373-396.

Dietterich, Thomas G. 2000. Ensemble methods in machine learning. Proc., International workshop on multiple classifier systems 1-15.

Dong, Hu and Blunt, Martin J. 2009. Pore-network extraction from micro-computerized-tomography images. *Physical review E* **80** (3): 036307.

Drexler, Wolfgang, Morgner, Uwe, Ghanta, Ravi K et al 2001. Ultrahigh-resolution ophthalmic optical coherence tomography. *Nature medicine* **7** (4): 502.

Dunlavy, Daniel, Kolda, Tamara G, and Kegelmeyer, W Philip. 2008. Tensor Decompositions for Analyzing Multi-link Graphs, Sandia National Lab. (SNL-NM), Albuquerque, NM (United States); Sandia ….

Ehrlich, Robert, Kennedy, Stephen K, Crabtree, Sterling J et al 1984. Petrographic image analysis; I, Analysis of reservoir pore complexes. *Journal of Sedimentary Research* **54** (4): 1365-1378.

Felzenszwalb, Pedro F and Huttenlocher, Daniel P. 2004. Efficient graph-based image segmentation. *International journal of computer vision* **59** (2): 167-181.

Ferreira, Tiago and Rasband, Wayne. 2012. ImageJ user guide. *ImageJ/Fiji* **1**: 155-161.

Gerke, Kirill M, Karsanina, Marina V, and Mallants, Dirk. 2015. Universal stochastic multiscale image fusion: an example application for shale rock. *Scientific reports* **5**: 15880.

Gonzalez, Rafael C, Woods, Richards E, and Eddins, Steven L. 2009. *Digital processing using MATLAB*, Gatesmark Publishing, Knoxville (Reprint).

He, Jianhua, Ding, Wenlong, Li, Ang et al 2016. Quantitative microporosity evaluation using mercury injection and digital image analysis in tight carbonate rocks: A case study from the Ordovician in the Tazhong Palaeouplift, Tarim Basin, NW China. *Journal of Natural Gas Science and Engineering* **34**: 627-644.

He, Kaiming, Zhang, Xiangyu, Ren, Shaoqing et al 2016. Deep residual learning for image recognition. Proc., Proceedings of the IEEE conference on computer vision and pattern recognition 770-778.

Huang, Bo, Wang, Wenqin, Bates, Mark et al 2008. Three-dimensional super-resolution imaging by stochastic optical reconstruction microscopy. *Science* **319** (5864): 810-813.

Jones, Stanley C. 1986. *System for measuring the pore volume and permeability of very tight core plugs and method therefor*, Google Patents (Reprint).

Jones, Stanley C. 1987. *Porous end plug disk for testing core samples*, Google Patents (Reprint).

Kann, Benjamin H, Thompson, Reid, Thomas Jr, Charles R et al 2019. Artificial Intelligence in Oncology: Current Applications and Future Directions. *Oncology* **33** (2).

Ketcham, Richard A and Iturrino, Gerardo J. 2005. Nondestructive high-resolution visualization and measurement of anisotropic effective porosity in complex lithologies using high-resolution X-ray computed tomography. *Journal of Hydrology* **302** (1-4): 92-106.

Knackstedt, MA, Arns, CH, Limaye, Ajay et al 2004. Digital Core Laboratory: Properties of reservoir core derived from 3D images. Proc., SPE Asia Pacific Conference on Integrated Modelling for Asset Management.

Knackstedt, MA, Arns, CH, Sheppard, AP et al 2007. Archie's exponents in complex lithologies derived from 3D digital core analysis. Proc., 48th Annual Logging Symposium.

Knecht, Leonora, Mathis, Benoit, Leduc, Jean-Pierre et al 2003. Electrofacies and permeability modeling in carbonate reservoirs using image texture analysis and clustering tools. Proc., SPWLA 44th annual logging symposium.

Kurz, Tobias H, Dewit, Julie, Buckley, Simon J et al 2012. Hyperspectral image analysis of different carbonate lithologies (limestone, karst and hydrothermal dolomites): the Pozalagua Quarry case study (Cantabria, North-west Spain). *Sedimentology* **59** (2): 623-645.

Li, Can, Hu, Miao, Li, Yunning et al 2018. Analogue signal and image processing with large memristor crossbars. *Nature Electronics* **1** (1): 52.

Li, Huiqi and Chutatape, Opas. 2004. Automated feature extraction in color retinal images by a model based approach. *IEEE Transactions on biomedical engineering* **51** (2): 246-254.

Lindeberg, Tony. 2015. Image matching using generalized scale-space interest points. *Journal of Mathematical Imaging and Vision* **52** (1): 3-36.

Lindquist, W Brent, Lee, Sang-Moon, Coker, David A et al 1996. Medial axis analysis of void structure in three-dimensional tomographic images of porous media. *Journal of Geophysical Research: Solid Earth* **101** (B4): 8297-8310.

Lindquist, WB and Venkatarangan, A. 1999. Investigating 3D geometry of porous media from high resolution images. *Physics and Chemistry of the Earth, Part A: Solid Earth and Geodesy* **24** (7): 593-599.

Liu, Zhe-Yu, Li, Yi-Qiang, Cui, Ming-Hui et al 2016. Pore-scale investigation of residual oil displacement in surfactant–polymer flooding using nuclear magnetic resonance experiments. *Petroleum Science* **13** (1): 91-99.

Lowe, David G. 2004. Distinctive image features from scale-invariant keypoints. *International journal of computer vision* **60** (2): 91-110.

Luffel, DL and Guidry, FK. 1992. New core analysis methods for measuring reservoir rock properties of Devonian shale. *Journal of Petroleum Technology* **44** (11): 1,184-1,190.

Malcolm, AA, Leong, HY, Spowage, AC et al 2007. Image segmentation and analysis for porosity measurement. *Journal of materials Processing technology* **192**: 391-396.

Marschall, D, Gardner, JS, Mardon, D et al 1995. Method for correlating NMR relaxometry and mercury injection data. Proc., 1995 SCA Conference, paper9511.

Mowers, Theodore T and Budd, David A. 1996. Quantification of porosity and permeability reduction due to calcite cementation using computer-assisted petrographic image analysis techniques. *AAPG bulletin* **80** (3): 309-321.

Müller, Andreas C and Guido, Sarah. 2016. *Introduction to machine learning with Python: a guide for data scientists*: "O'Reilly Media, Inc.".

Pedregosa, Fabian, Varoquaux, Gaël, Gramfort, Alexandre et al 2011. Scikit-learn: Machine learning in Python. *Journal of machine learning research* **12** (Oct): 2825-2830.

Polakowski, William E, Cournoyer, Donald A, Rogers, Steven K et al 1997. Computer-aided breast cancer detection and diagnosis of masses using difference of Gaussians and derivative-based feature saliency. *IEEE transactions on medical imaging* **16** (6): 811-819.

Polan, Daniel F, Brady, Samuel L, and Kaufman, Robert A. 2016. Tissue segmentation of computed tomography images using a Random Forest algorithm: a feasibility study. *Physics in Medicine & Biology* **61** (17): 6553.

Rafael, Gonzalez C, Richard, Woods E, and Steven, Eddins L. 2007. Digital image processing 3rd edition. *Eighth Impression*.

Rasmussen, Carl Edward. 2003. Gaussian processes in machine learning. Proc., Summer School on Machine Learning 63-71.

Russ, John C. 2016. *The image processing handbook*: CRC press.

Sánchez, Clara I, Hornero, Roberto, López, María I et al 2008. A novel automatic image processing algorithm for detection of hard exudates based on retinal image analysis. *Medical engineering & physics* **30** (3): 350-357.

Saxena, Nishank, Mavko, Gary, Hofmann, Ronny et al 2017. Estimating permeability from thin sections without reconstruction: Digital rock study of 3D properties from 2D images. *Computers & Geosciences* **102**: 79-99.

Schindelin, Johannes, Arganda-Carreras, Ignacio, Frise, Erwin et al 2012. Fiji: an open-source platform for biological-image analysis. *Nature methods* **9** (7): 676.

Shattuck, David W, Sandor-Leahy, Stephanie R, Schaper, Kirt A et al 2001. Magnetic resonance image tissue classification using a partial volume model. *NeuroImage* **13** (5): 856-876.

Simonyan, Karen and Zisserman, Andrew. 2014. Very deep convolutional networks for large-scale image recognition. *arXiv preprint arXiv:14091556*.

Singh, Kamaljit, Menke, Hannah, Andrew, Matthew et al 2017. Dynamics of snap-off and pore-filling events during two-phase fluid flow in permeable media. *Scientific reports* **7** (1): 5192.

Sommer, Christoph, Straehle, Christoph, Koethe, Ullrich et al 2011. Ilastik: Interactive learning and segmentation toolkit. Proc., 2011 IEEE international symposium on biomedical imaging: From nano to macro 230-233.

Wang, Haitao, Lun, Zengmin, Lv, Chengyuan et al 2017. Measurement and visualization of tight rock exposed to CO 2 using NMR relaxometry and MRI. *Scientific reports* **7**: 44354.

Wang, Yunzhi, Aghaei, Faranak, Zarafshani, Ali et al 2017. Computer-aided classification of mammographic masses using visually sensitive image features. *Journal of X-ray Science and technology* **25** (1): 171-186.

Wilson, Kevin. 2014. Microsoft office 365. In *Using office 365*, 1-14. Springer.

Xu, Hao, Tang, Dazhen, Zhao, Junlong et al 2015. A precise measurement method for shale porosity with low-field nuclear magnetic resonance: A case study of the Carboniferous–Permian strata in the Linxing area, eastern Ordos Basin, China. *Fuel* **143**: 47-54.

Yang, Jianchao, Wright, John, Huang, Thomas S et al 2010. Image super-resolution via sparse representation. *IEEE transactions on image processing* **19** (11): 2861-2873.

Yu, Ruiyun, Yang, Yu, Yang, Leyou et al 2016. RAQ–a random forest approach for predicting air quality in urban sensing systems. *Sensors* **16** (1): 86.

Zhang, Yan, Passmore, Peter J, and Bayford, Richard H. 2006. Visualization and Post-processing of 5D brain images. Proc., 2005 IEEE Engineering in Medicine and Biology 27th Annual Conference 1083-1086.

Zhou, Qi You, Shimada, Jun, and Sato, Akira. 2001. Three-dimensional spatial and temporal monitoring of soil water content using electrical resistivity tomography. *Water Resources Research* **37** (2): 273-285.